RSC Advances

PAPER

View Article Online
View Journal | View Issue

Cite this: *RSC Adv.*, 2023, **13**, 26196

Lanthanide-MOFs as multi-responsive photoluminescence sensor for sensitively detecting Fe^{3+}, $Cr_2O_7^{2-}$ and nitrofuran antibiotics†

Jingjuan Feng,‡[a] Cunding Kong,‡[a] Yunhui Chen,[a] Peipei Cen, *[b] Yi Ding,[a] Yan Guo,[a] Fengyuan Zhang[b] and Xiangyu Liu *[a]

Received 7th June 2023
Accepted 16th August 2023

DOI: 10.1039/d3ra03817c

rsc.li/rsc-advances

Fast and selective detection of contaminants plays a key role in meeting human health and environmental concerns. Herein, two groups of isostructural lanthanide MOFs, [Ln(Hpta)(oxalic acid)]·H_2O (**1**-Eu, **2**-Gd) and [Ln(pta)(oxalic acid)$_{0.5}$(H_2O)$_2$]·2H_2O (**3**-Eu, **4**-Gd) (H_2pta = 2-(4-pyridyl)-terephthalic acid, $C_2O_4^-$ = oxalic acid), were synthesized by solvothermal method. Single crystal X-ray diffraction reveals that **1** and **2** are 3D neutral frameworks, while **3** and **4** consist of 2D layers with parallelogram holes and stack into 3D networks through O–H···N and O–H···O hydrogen bonding interactions. All complexes remain crystalline and stable below 400 °C, suggesting preeminent thermostability. Noteworthily, only **3** shows excellent chemical stability in water and organic solvent. Therefore, the solid-state fluorescence spectrum was used to characterize **3** which exhibited intense red luminescence. The N active sites in the pore channels of **3** are conducive to displaying a distinct quenching effect for Fe^{3+} cations in aqueous solutions, $Cr_2O_7^{2-}$ anions in DMF and DMA solutions, and nitrofuran antibiotics in the DMF solvent. Overall, **3** is a prospective luminescent sensor for detecting Fe^{3+}, $Cr_2O_7^{2-}$ and nitrofuran antibiotics.

Introduction

In recent years, the effective detection of heavy metal ions, inorganic ions and antibiotics has become paramount to regions spanning the globe to protect human health and homeland security.[1–3] Now, among the various detection methods, fluorescence-based chemical sensor systems are gaining increasing attention for the detection of nitrofuran antibiotics, inorganic anions and heavy metal ionic substances.[4–7]

In recent years, luminescent functional metal–organic framework (MOF) materials acting as fluorescent probes have attracted extensive attention.[8–10] In comparison to transition metal ions, lanthanide ions possess higher coordination numbers, flexible coordination geometry and narrow emissions, which affect the structural diversity and luminescent properties of Ln-MOFs.[11,12] Ln-MOFs impart tunable functionality and designable topology and exhibit unique luminescence properties, including large Stokes shifts, narrow bandwidth, high colour purity and relatively long luminescence lifetimes.[13] Furthermore, because the 4f transitions of lanthanide ions are inner-shell transitions and the emission spectra display narrow bandwidths ($\Delta\lambda$ < 10 nm), they have been extensively explored for applications in lighting, displays, sensing, and optical devices. These intrinsic luminescence features of lanthanides together with the unique advantages of MOFs offer hopeful prospects for designing novel luminescent materials.[14] However, the majority of Ln-MOFs are still unstable in water and organic solvents, as observed with other MOFs, which is mainly attributed to the weak coordinated bond in the coordinated structure.[15,16] Accordingly, it is of great significance to design and prepare ultrastable Ln-MOFs for highly selective and sensitive luminescence sensing for antibiotics and heavy metal ion substances in solutions.

Organic ligands, usually acting as building blocks in the assembly of MOFs, help to determine the backbones as well as the functions of these materials. What is noteworthy is that most MOFs in luminescence sensing are synthesized using aromatic carboxylate or pyridyl–carboxylate linkers.[17] Pyridyl ligands containing a nitrogen donor are incorporated in MOFs, beneficially increasing the interactive water stability of MOFs.[18] Obviously, the versatile pyridyl-decorated dicarboxylic 2-(4-pyridyl)-terephthalic acid (H_2pta) will be a promising candidate to afford multifunctional MOFs due to the following points: (1) H_2pta contains a pyridyl ring and a phenyl ring with structural flexibility and conformational freedom. Rotation of the C–C

[a]*State Key Laboratory of High-efficiency Utilization of Coal and Green Chemical Engineering, College of Chemistry and Chemical Engineering, Ningxia University, Yinchuan 750021, China. E-mail: xiangyuliu432@126.com*

[b]*College of Public Health, College of Basic Medical Science, Ningxia Medical University, YinChuan 750021, China. E-mail: 13895400691@163.com*

† Electronic supplementary information (ESI) available: Fig. S1–S15, Tables S1–S3, crystal structures in CIF format. CCDC 2180904 (**1**), 2180910 (**2**), 2180911 (**3**) and 2180912 (**4**). For ESI and crystallographic data in CIF or other electronic format see DOI: https://doi.org/10.1039/d3ra03817c

‡ These authors contributed equally to this work.

single bond between the pyridyl and phenyl rings could form a number of coordination geometries of metal ions. (2) It has two carboxyl groups that may be completely or partially deprotonated, inducing rich coordination modes and allowing interesting structures with higher dimensionalities. (3) The potential uncoordinated pyridyl N atoms as functional sites could recognize Lewis acidic metal ions. These characteristics of the H_2pta ligand may lead to cavities, interpenetration, helical structures, and other novel motifs with unique topologies.[19–21] Besides, the advantages of the mixed ligand strategy inspire us to introduce other versatile bridging linkers into the reaction system, to act in structural modulation, bridging pillar, or charge balance roles,[22] whose particular behaviors allow them to be potential components for designing frameworks with diverse networks and functionalities.

Based on the above considerations, difunctional 2-(4-pyridyl)-terephthalic acid (H_2pta) is employed as an organic linker with lanthanide ions to construct Ln(III)-MOFs with magnificent architectures and fascinating functions. Two groups of new isostructural Ln(III)-MOFs, $[Ln(Hpta)(C_2O_4)]\cdot H_2O$ (**1**-Eu, **2**-Gd) and $[Ln(pta)(C_2O_4)_{0.5}(H_2O)_2]\cdot 2H_2O$ (**3**-Eu, **4**-Gd), were obtained with the help of the oxalic acid coligand *via* hydrothermal reaction (Scheme 1). The crystallographic structures, thermostabilities, and chemical stabilities of these MOFs were characterized. Interestingly, complex **3** shows a highly selective luminescence quenching action for Fe^{3+} cations in aqueous media, $Cr_2O_7^{2-}$ anions in DMF and DMA solutions and nitrofuran antibiotics in DMF solvent. The good reproducibility and remarkable selectivity of **3** makes it a promising candidate for chemical sensor.

Experimental

Materials and physical measurements

All commercially available chemicals were used without further purification. Elemental analysis (C, H, and N) was performed using a PerkinElmer 2400 CHN elemental analyzer. An EQUINOX55 FT/IR spectrometer was used to record Fourier-transform infrared spectroscopy (FT-IR) spectra in the range of 400–4000 cm^{-1} using KBr pellets.[23] The phase purity of the bulk or polycrystalline samples was examined by powder X-ray diffraction (PXRD) measurements performed on a Rigaku RU20 diffractometer at 60 kV and 300 mA using Cu Kα radiation ($\lambda = 1.5406$ Å) with a scanning speed of 5° min^{-1} and a step size of 0.02° in 2θ. Thermal gravimetric analysis (TGA) was performed using a NETZSCH STA 449F3 instrument at a heating rate of 10 °C min^{-1} from 25 to 900 °C under a N_2 stream using an empty Al_2O_3 crucible as the standard. The fluorescence spectra were obtained using a Hitachi F-7000 fluorescence spectrophotometer at room temperature. UV-Vis spectroscopic studies were collected on a Shimadzu WFH-203B spectrophotometer.

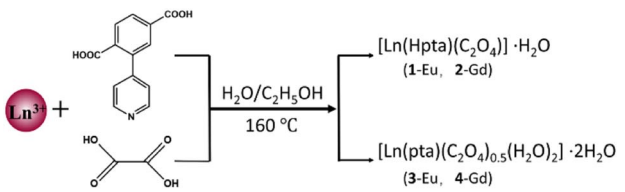

Scheme 1 Synthetic route of complexes **1–4**.

Synthesis procedures of complexes

Complexes **1** and **2** were synthesized by the following methods. A mixture of H_2pta (0.025 mmol), Ln $(NO_3)_3\cdot 6H_2O$ (Ln = Eu, Gd) (0.05 mmol) and oxalic acid (0.05 mmol) was dissolved in 8 mL of CH_3CH_2OH/H_2O (1 : 1) in a 15 mL vial, heated in a Teflon-lined stainless-steel vessel at 160 °C for 3 days and then cooled at a rate of 3 °C h^{-1} to room temperature. Colorless needle-shaped crystals were collected by filtration and dried in air. The procedures for complexes **3** and **4** were the same as those for **1** and **2** except that the CH_3CH_2OH/H_2O (1 : 1) was replaced by 1 : 7. Colorless block crystals were obtained and collected by filtration.

$[Eu(Hpta)(C_2O_4)]\cdot H_2O$ (1). Yield of 55.0% (based on Eu^{3+}). Anal. (%) calcd for $C_{15}H_{10}NO_9Eu$: C, 36.02; H, 2.02; N, 2.80. Found: C, 35.98; H, 1.96; N, 2.75. IR (KBr pellet, cm^{-1}): 3410(s), 2976(w), 1636(m), 1580(s), 1534(s), 1508(s), 1421(s), 1374(s), 1342(s), 1094(w), 840(m), 808(m), 570(m).

$[Gd(Hpta)(C_2O_4)]\cdot H_2O$ (2). Yield of 45.0% (based on Gd^{3+}). Anal. (%) calcd for $C_{15}H_{10}NO_9Gd$: C, 35.64; H, 1.99; N, 2.77. Found: C, 34.88; H, 1.76; N, 2.45. IR (KBr pellet, cm^{-1}): 3426(s), 2976(m), 1630(m), 1580(m), 1536(m), 1510(m), 1420(m), 1380(m), 1318(m), 1094(w), 804(m), 720(m), 578(m).

$[Eu(pta)(C_2O_4)_{0.5}(H_2O)_2]\cdot 2H_2O$ (3). Yield of 49.0% (based on Eu^{3+}). Anal. (%) calcd for $C_{14}H_{15}NO_{10}Eu$: C, 33.02; H, 2.97; N, 2.75. Found: C, 32.89; H, 2.83; N, 2.56. IR (KBr pellet, cm^{-1}): 3340(s), 1670(m), 1552(s), 1430(s), 1381(m), 1322(m), 860(m), 779(m), 597(w).

$[Gd(pta)(C_2O_4)_{0.5}(H_2O)_2]\cdot 2H_2O$ (4). Yield of 53.0% (based on Gd^{3+}). Anal. (%) calcd for $C_{14}H_{15}NO_{10}Gd$: C, 32.68; H, 2.94; N, 2.72. Found: C, 32.48; H, 2.78; N, 2.65. IR (KBr pellet, cm^{-1}): 3342(s), 1667(m), 1550(s), 1429(s), 1379(m), 1320(m), 857(m), 777(m), 599(w).

Crystallographic data collection and refinement

Suitable single crystals of all complexes were selected for X-ray measurements. Crystal structures were collected with a Bruker D8 VENTURE X-ray CMOS diffractometer using graphite monochromated Cu-K_α radiation ($\lambda = 154\,178$ Å) at 150 K for **1** and **2** and Mo-K_α X-ray radiation ($\lambda = 0.71073$ Å) at 100 K for **3** and **4**. The structures were determined by direct methods and refined against F^2 by full-matrix least squares with Olex 2.3. All non-hydrogen atoms were refined with anisotropic thermal parameters. All hydrogen atoms were placed in calculated positions and refined isotropically. For both **1** and **2**, the diffraction contribution of the highly disordered solvent molecules located in the structure was eliminated by applying the program SQUEEZE implemented in PLATON. Crystallographic data and structural refinement details for **1–4** are summarized in Table S1.† Selected bond lengths and bond angles are listed in Table S2.† Crystallographic data from the structural analysis have

been deposited with the Cambridge Crystallographic Data Centre. The CCDC numbers are 2180904 (**1**), 2180910 (**2**), 2180911 (**3**) and 2180912 (**4**).

Results and discussion

Crystal structures of 1–4

Since the crystallographic analysis reveals that complexes **1** and **2** and complexes **3** and **4** are isomorphous, we chose complexes **1** and **3** as representatives to describe the detailed structures. Complex **1** crystallizes in the monoclinic $P2_1/c$ space group and exhibits a 3D skeleton. As shown in Fig. S1a,† the asymmetric unit is composed of one independent Eu^{3+} ion, one $Hpta^-$ ligand, one coordinated $C_2O_4^{2-}$ and free H_2O molecules. The Eu^{3+} ion is eight-coordinated by four oxygen atoms (O5, O6A, O7A and O8) from $C_2O_4^{2-}$ and four carboxylate oxygen atoms (O1B, O2, O3A and O4A) from three different pta^{2-} ligands, indicating a distorted trigonal prismatic geometry (Fig. 1a). Two carboxylic groups in the $Hpta^-$ ligand link with three Eu^{3+} centers in bridging and chelating modes, respectively (Fig. 1b). Herein, two neighboring Eu^{3+} ions are connected by two μ_2-COO^- groups to produce a binuclear secondary building unit (SBU) (Fig. 1c). The SBUs are joined by $Hpta^-$ ligands to form an infinite one-dimensional (1D) chain as displayed in Fig. 1d. The $C_2O_4^{2-}$ ligand links the adjacent chains to obtain a two-dimensional (2D) layer which is further enlarged by the $C_2O_4^{2-}$ ligands to engender a 3D porous framework (Fig. 2a and b). The structure of complex **2** is shown in Fig. S1b, S2 and S3.† Complex **3** possesses a 2D framework in the triclinic space group $P\bar{1}$. The asymmetric unit of **3** consists of one Eu^{3+} ion, one pta^{2-} ligand with the protonation of oxygen atom, a half coordinated $C_2O_4^{2-}$ ligand, two coordinated H_2O molecules and free H_2O molecules (Fig. 3a). As shown in Fig. S1c,† the nine-coordinated Eu^{3+} ions are surrounded by nine O atoms to generate a muffin geometry, in which five O atoms (O1, O1A, O2A, O3B, O4B) stem from three carboxyl groups of three different pta^{2-} ligands, two O atoms (O5, O6) come from $C_2O_4^{2-}$ ligands and two oxygen atoms (O7W, O8W) come from coordinated water molecules. Two carboxylate groups of each pta^{2-} ligand link with three Eu^{3+} centers as bridging/chelating tridentate and chelating bidentate (Fig. 3b). Two Eu^{3+} centers are connected by a pair of μ_3-O atoms to form an edge-sharing $Eu_2(COO)_2$ unit and the adjacent $Eu_2(COO)_2$ units are linked by the pta^{2-} backbones, leading to a 1D double chain (Fig. 3c). The coordination bonds between the Eu^{3+} ions and pta^{2-} ligands cause the generation of 2D layers (Fig. 3d). Each layer is stacked through the hydrogen bonds of coordinated water molecules (Fig. 4a) and the stacking of layers forms a 3D supramolecular structure (Fig. 4b). The structure of complex **4** is shown in Fig. S1d, S4 and S5.†

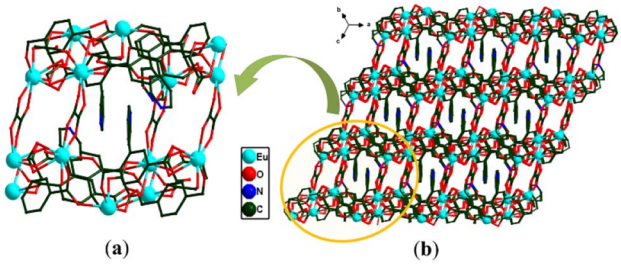

Fig. 2 (a) Layer structure and (b) 3D structure of **1**.

Powder X-ray diffraction (PXRD) and thermogravimetry (TG)

To confirm the phase purity of the obtained products, powder X-ray diffraction (PXRD) experiments were carried out for complexes **1–4**. The measured PXRD results match the simulated patterns based on the single crystal data, suggesting the high phase purity and crystallinity of **1–4** (Fig. S6†).

The TG curves (Fig. S7†) of **1–4** were obtained by thermogravimetric tests under N_2 atmosphere. On account of the isomorphism of **1** and **2**, as well as **3** and **4**, the TG curves of **1** and **3** are described as respective representatives. For **1**, the weight loss of 3.32% at 25–97 °C (theoretical value is 3.60%) is

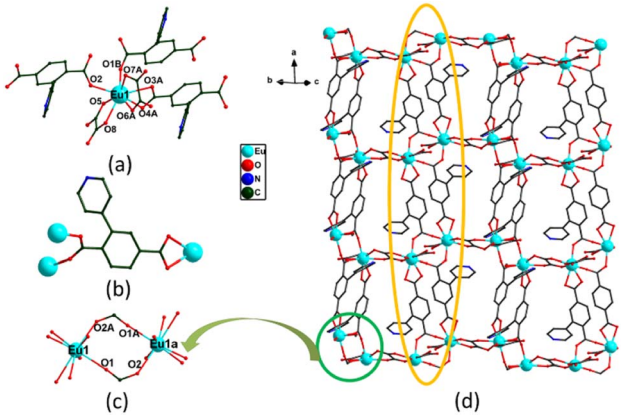

Fig. 1 (a) The coordination environment of Eu^{3+} in **1**; (b) the coordination modes of pta^{2-} in **1**; (c) the dinuclear $[Eu_2(COO)_2]$ cluster; (d) a view of the 2D structure of **1** (Eu cyan, O red, N blue, C grey, hydrogen atoms omitted for clarity).

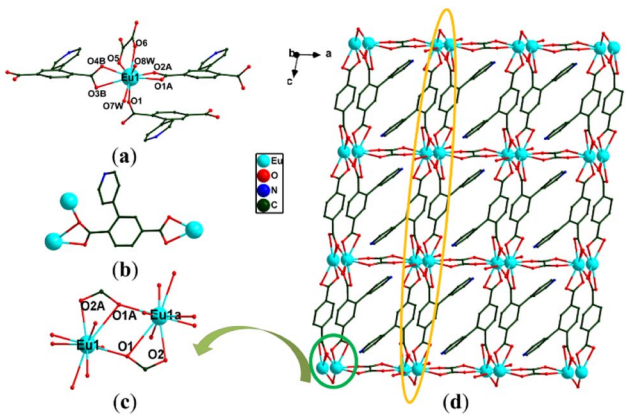

Fig. 3 (a) The coordination environment of Eu^{3+} in **3**; (b) the coordination modes of pta^{2-} in **3**; (c) the dinuclear $[Eu_2(COO)_2]$ cluster; (d) a view of the 2D structure of **3** (Eu cyan, O red, N blue, C grey, hydrogen atoms omitted for clarity).

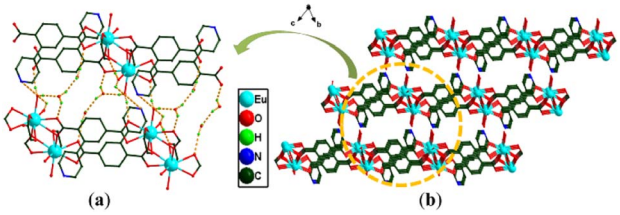

Fig. 4 (a) Layer structure and (b) 3D structure of **3**.

due to the loss of free water molecules. The weight loss of 17.55% from 97 to 470 °C is consistent with the removal of the oxalic acids (theoretical value is 17.99%). Above 474 °C, the framework of complex **1** collapses. In the case of **3**, the weight loss of 7.99% below 124 °C relates to the removal of free water molecules (calcd 7.07%). The weight loss of 3.62% in the temperature range of 181–218 °C is attributed to the disappearance of coordinated water molecules (calcd 3.53%). Above 418 °C, the main framework of complex **3** decomposes rapidly.

Chemical stability

Further exploring the chemical stability of **1–4** is significant to practical applications. Unfortunately, the chemical stabilities of complexes **1**, **2** and **4** were unqualified. In contrast, the peak positions of the PXRD patterns for **3** remain basically unchanged after immersion in water for seven days (Fig. 5a), in both acidic and basic solutions (pH = 4–11) (Fig. 5b), and even in common organic solvents (Fig. 5c) for 24 h at room temperature, indicating that **3** could remain stable in water, acidic/basic solutions and organic solvents.[24]

Fluorescence properties

In this case, the luminescent properties of H_2pta and **3** were also investigated. As shown in Fig. S8 and S9,† the luminescence spectrum of **3** reveals characteristic photoluminescence properties with fluorescence peaks at 550, 598, and 623 nm which are attributed to the $^5D_0 \rightarrow {}^7F_1$, $^5D_0 \rightarrow {}^7F_2$, and $^5D_0 \rightarrow {}^7F_4$ transitions of Eu^{3+} ions, respectively (excitation wavelength 315 nm). From the Eu^{3+} transition rules, if Eu^{3+} ions take up an inversion center, orange light is emitted from the magnetic dipole transitions ($^5D_0 \rightarrow {}^7F_1$) and if Eu^{3+} ions take up a non-inversion center, red light is emitted because of the electric dipole transitions ($^5D_0 \rightarrow {}^7F_2$). However, the luminescence intensity of **3** at 623 nm ($^5D_0 \rightarrow {}^7F_2$ transitions) is stronger than that at 598 nm ($^5D_0 \rightarrow {}^7F_1$ transitions), which indicates that Eu^{3+} ions take up a non-inversion center. This transition is comparable to earlier reported luminescence studies of Eu-based MOFs.[25]

Detection of metal ions

Based on the excellent luminescence properties and structural stability of complex **3**, subsequent fluorescence sensing experiments were performed. The powder samples were immersed in 0.01 mol L^{-1} of various $M(NO_3)_x$ ($M = K^+$, Na^+, Ni^{2+}, Co^{2+}, Pb^{2+}, Zn^{2+}, Cu^{2+}, Cd^{2+}, Ag^+, Ca^{2+} and Fe^{3+}) aqueous, DMF, DMA, EtOH, MeOH, and CH_3CN solutions. The results are shown in Fig. 6a and b. Only Fe^{3+} ions show a distinct quenching effect on the luminescence of complex **3** in aqueous solutions. In order to confirm the selectivity, more experiments were performed. When Fe^{3+} and other metal ions (Zn^{2+}, Pb^{2+}, Ni^{2+}, Co^{2+}, Na^+, Cu^{2+}, Cd^{2+}) with mixed ratios of 1 : 3 were added to the solution, the fluorescence was completely quenched as well. The results further demonstrate the excellent anti-interference ability of **3** in the detection of Fe^{3+} (Fig. S10†). Furthermore, a series of titration experiments was carried out in aqueous solutions with various concentrations of Fe^{3+}. The fluorescence intensity of **3** (Fig. 6c) is almost entirely quenched when the Fe^{3+} concentration is 500 mM. Quantitatively, the quenching efficiency is calculated using the Stern–Volmer (S–V) equation: $(I_0/I) = 1 + K_{sv}[Q]$, where I_0 and I are the luminescence intensities before and after adding metal ions, respectively, [Q] refers to the molar concentration of metal ions and K_{sv} is the quenching constant, which is an important indicator of the sensing ability of a fluorescent sensor. The K_{sv} value is found to be 1.96×10^4 M^{-1} for **3**

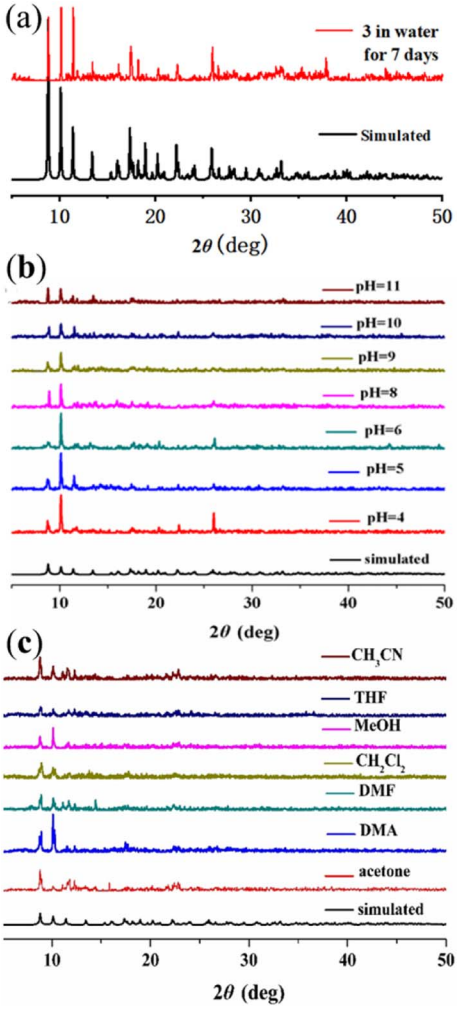

Fig. 5 PXRD profiles of **3** after being soaked in (a) water for seven days, (b) acidic and basic solutions for 24 h, and (c) different organic solvents for 24 h.

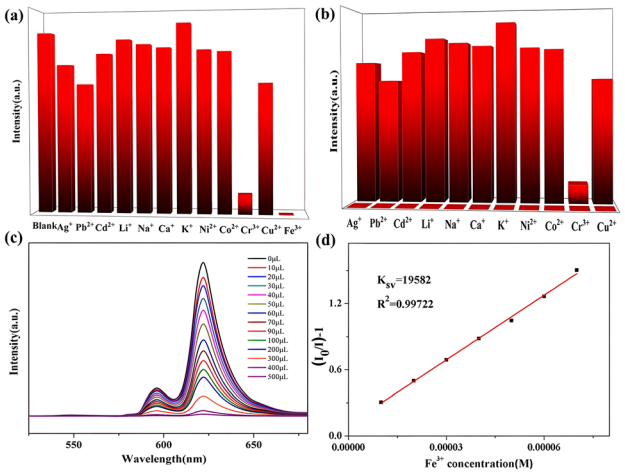

Fig. 6 (a) Luminescence intensity (315 nm excitation wavelength) of **3** treated with 0.01 M of various different metal ions in water; (b) luminescence intensity at 315 nm of **3** dispersed in water with the addition of different ions (0.01 M) (Cu^{2+}, Ag^{+}, Zn^{2+}, Na^{+}, Pb^{2+}, Co^{2+}, K^{+}, Cd^{2+}, Ca^{2+}, Ni^{2+}, Li^{+}) and Fe^{3+} incorporated systems (0.01 M); (c) luminescence spectra of **3** in aqueous solutions with Fe^{3+} at different concentrations; (d) a plot of relative luminescence intensity *vs.* Fe^{3+} concentration.

(Fig. 6d), signifying that Fe^{3+} has a high-efficiency quenching effect on the luminescence emission of **3**. According to the ratio of $3\delta/K_{sv}$ (δ: standard error), the detection limit is 3.25×10^{-5} M for **3**. In fact, complex **3** possesses selectivity for both Fe^{3+} and Cu^{2+} in organic solvents. The titration experiments and K_{sv} results are shown in Fig. S11–S14.† Furthermore, **3** (Fig. 7a) was washed with water several times and the fluorescence intensities were well-retained over five runs. Meanwhile, the PXRD patterns prove that the crystallinity and structural integrity of **3** (Fig. 8a) exhibit no change after the detection tests, supporting its good recyclability. Overall, the high sensitivity and recyclability for Fe^{3+}, together with its stability in acidic/basic aqueous solutions, make **3** competitive compared to other MOF fluorescent probes.

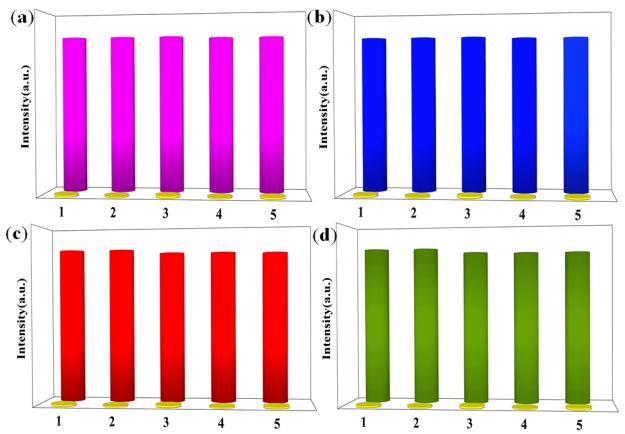

Fig. 7 (a) Recyclability of the quenching ability of **3** immersed in water and in the presence of 0.01 M aqueous solution of Fe^{3+} ions; (b) recyclability of the quenching ability of **3** immersed in DMF and in the presence of 0.01 M DMF solution of NFT; (c) recyclability of the quenching ability of **3** immersed in DMF and in the presence of 0.01 M DMF solution of $Cr_2O_7^{2-}$ anions; (d) recyclability of the quenching ability of **3** immersed in DMA and in the presence of 0.01 M DMA solution of $Cr_2O_7^{2-}$ anions (the purple/blue/red/green columns represent the initial fluorescence intensity and the yellow columns represent the intensity upon the addition of an aqueous solution of 0.01 M Fe^{3+}/NFT/$Cr_2O_7^{2-}$).

Detection of antibiotics

To explore the ability of **3** to sense trace quantities of antibiotics, fluorescence-quenching titrations were performed with the addition of antibiotics to DMF in which **3** was dispersed. A total of eight frequently used antibiotics, nitrofurantoin (NFT), nitrofurazone (NFZ), sulfachloropyridazine (SCP), sulfamethoxazole (SMZ), trimethoprim (TMP), penicillin sodium (PCL), and morpholine guanidine hydrochloride (MH), were added. As shown in Fig. 9a, NFT and NFZ, both nitrofuran antibiotics, have the highest quenching efficiency for **3**. The quenching efficiencies for **3** of these antibiotics follow the order NFT > NFZ > SCP > SMZ > TMP > MH > PCL. Thus, **3** is a promising luminescent probe for the selective detection of nitrofuran antibiotics. Subsequently, the fluorescence sensing performance of **3** towards NFT inspired us to check the anti-interference ability for NFT detection. Fluorescence titration experiments were performed (Fig. 9b). From the linear fitting of the S–V plot, the calculated K_{sv} value for NFT is 4.01×10^4 M^{-1} (Fig. 9c). According to $3\delta/K_{sv}$, the calculated detection limit for NFT is 2.69×10^{-5} M. To evaluate the recyclability of **3**, cyclic luminescence tests were performed and the fluorescence intensity of **3** was observed to have little variation after the sample was washed with fresh DMF several times (Fig. 7b and 8b). The results demonstrate that **3** is an ideal fluorescence sensor for detecting nitrofuran antibiotics with high sensitivity, good recyclability and superior anti-interference capability.

Detection of anions

In addition, **3** was also used for the detection of anions in industrial wastewater. It was dispersed into DMF, DMA, EtOH, MeOH, and CH_3CN solutions containing potassium salts of NO_3^-, PO_4^{3-}, SO_4^{2-}, Br^-, $S_2O_8^{2-}$, CrO_4^{2-}, HPO_4^{2-} and $Cr_2O_7^{2-}$ at the same concentration to study their effects on the luminescent intensity of this MOF. The luminescent measurements clearly illustrate that Fe^{3+}, Cu^{2+}, and $Cr_2O_7^{2-}$ could cause fluorescence quenching for **3** in different organic solvents (Table

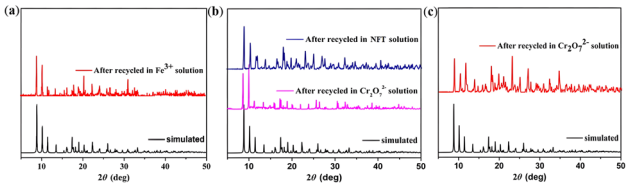

Fig. 8 (a) PXRD patterns of **3** treated by Fe^{3+} aqueous solution; (b) PXRD patterns of **3** treated by NFT/$Cr_2O_7^{2-}$ in DMF solution; (c) PXRD patterns of **3** treated by $Cr_2O_7^{2-}$ in DMA solution.

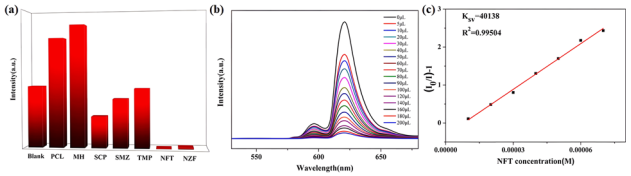

Fig. 9 (a) Luminescence intensity (315 nm excitation wavelength) of **3** treated with 0.01 M of various different antibiotics in DMF; (b) luminescence spectrum of **3** in DMF with NFT at different concentrations; (c) a plot of relative luminescence intensity *vs.* NFT concentration.

S3†). Remarkably, $Cr_2O_7^{2-}$ gives rise to the highest quenching effect on the emission of complex **3** in DMA and DMF solutions (Fig. 10a and S15a†). Meanwhile, the selectivity was tested and the sensing results in organic solvents are shown in Fig. 10b and S15b.†

The fluorescence emission was still remarkably quenched with the addition of $Cr_2O_7^{2-}$, clearly confirming that the other anions could not interfere with the $Cr_2O_7^{2-}$ sensing. In addition, a series of titration experiments were carried out in DMA and DMF solutions with various concentrations of $Cr_2O_7^{2-}$. The fluorescence intensities for **3** (Fig. 10c and S15c†) are almost entirely quenched at $Cr_2O_7^{2-}$ ion concentrations of 1200 μL in DMA solution and 700 μL in DMF solution. The K_{sv} values are found to be 1.85×10^4 M^{-1} and 8.47×10^3 M^{-1} for **3** (Fig. 10d and S15d†), showing that $Cr_2O_7^{2-}$ has a high-efficiency quenching effect on the luminescence emission of **3**, and the detection limits calculated by $3\delta/K_{sv}$ are 1.3×10^{-5} M and 6.67×10^{-5} M. Recycling experiments were also recorded for **3** which was washed with acetone solution several times (Fig. 7c and d). The PXRD (Fig. 8b and c) and luminescence intensity curves of the recycled **3** are well consistent with the original results,

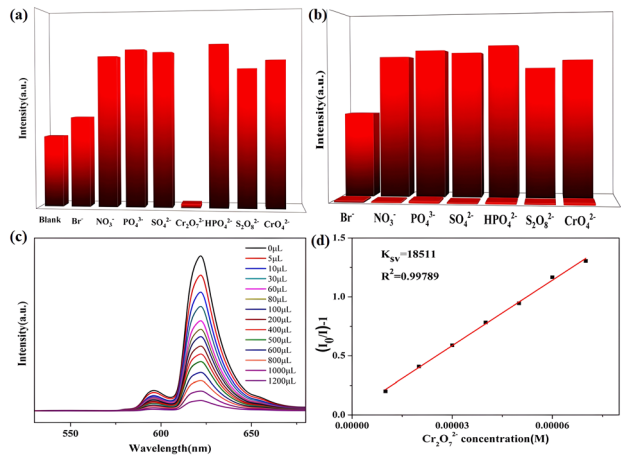

Fig. 10 (a) Luminescence intensity (315 nm excitation wavelength) of **3** treated with 0.01 M of various different anions in DMA; (b) luminescence intensity (315 nm) of **3** dispersed in DMA with the addition of different anions (0.01 M) (NO^{3-}, CrO_4^{2-}, Br^-, SO_4^{2-}, $S_2O_8^{2-}$, PO_4^{3-}, HPO_4^{2-}) and $Cr_2O_7^{2-}$ incorporated systems (0.01 M); (c) luminescence spectrum of **3** in DMA solutions with $Cr_2O_7^{2-}$ at different concentrations; (d) a plot of relative luminescence intensity *vs.* $Cr_2O_7^{2-}$ concentration.

proving that **3** as a $Cr_2O_7^{2-}$ probe can be recycled with a fast and simple method. In addition, complex **3** possesses selectivity for $S_2O_8^{2-}$ and $Cr_2O_7^{2-}$ in aqueous solvents (Fig. S16†).

Mechanism for sensing of Fe^{3+}, NFT, and $Cr_2O_7^{2-}$

The mechanism of the fluorescence quenching of **3** caused by metal ions, anions and nitro antibiotics is explained by analyzing the ultraviolet absorption spectra (UV-Vis) of the target products and complex **3**.[26] The PXRD patterns for **3** before and after the fluorescence experiments are consistent with each other, excluding the possibility of the luminescence quenching effect being derived from the collapse of the framework (Fig. 8). The experimental data indicate that strong absorption bands appear in the UV-Vis absorption spectrum (200–250 nm) of Fe^{3+} in aqueous solution, while the excitation wavelength of **3** is 315 nm (Fig. S17a†), suggesting that the fluorescence quenching is not caused by competition absorption of the excitation wavelength energy between Fe^{3+} and complex **3**. According to Fig. S18,† the fluorescence lifetime of **3** reduced from 0.568 ns to 0.401 ns after adding Fe^{3+}, indicated that the fluorescence quenching effect is dynamic quenching.[27] The UV-Vis absorption spectra of $Cr_2O_7^{2-}$ in DMF and DMA solutions and NFT in DMF solution show strong absorption bands for $Cr_2O_7^{2-}$ in DMF (250–300 and 300–400 nm), $Cr_2O_7^{2-}$ in DMA (300–315 and 315–450 nm), and NFT (250–305 and 305–450 nm) and the excitation wavelength for **3** is 315 nm (Fig. S17b–d†). From the experimental data, the UV-Vis absorption spectra of $Cr_2O_7^{2-}$ and NFT overlap with the excitation spectrum of **3**. These facts imply that $Cr_2O_7^{2-}$ and NFT could absorb the energy of the excitation light from **3**, reducing the efficiency of the energy transformation from the ligand to the lanthanide ions, which definitely induces the luminescence quenching effect. In addition, the uncoordinated pyridine groups can be used as functional groups to detect metal ions and small organic molecules,[28] so the N active sites in the pore channel of **3** may be beneficial to promote the selectivity and sensitivity for detecting Fe^{3+} cations, $Cr_2O_7^{2-}$ anions and nitrofuran antibiotics.

Conclusion

In conclusion, four new paired MOFs assembled from 2-(4-pyridyl)-terephthalic acid have been successfully isolated and structurally characterized. Particularly, complex **3**, which contains Eu^{3+} ions nine-coordinated in muffin geometry, shows excellent stability and luminescence properties. This Eu(III) based MOF presents the potential for highly sensitive and selective detection of Fe^{3+} in water and NZF in DMF solution, as well as $Cr_2O_7^{2-}$ in DMF and DMA solutions. The possible mechanism is fluorescence quenching dependent on competitive absorption between complex **3** and the analytes. The successful assembly of the present case may provide a good guideline to construct new Eu(III)-MOF functional materials.

Conflicts of interest

There are no conflicts of interest to declare.

Acknowledgements

This work was supported by the NSFC (21863009 and 22063008), the Natural Science Foundation of Ningxia Province (2023AAC03227, 2022AAC05002, 2021AAC03136 and 2021BEB04062), the Young Top-notch Talent Cultivation Program of Ningxia Province, the Discipline Project of Ningxia (NXYLXK2017A04), the China Postdoctoral Science Foundation (2022M723148) and the Research Project of Ningxia Medical University (XT2019001).

Notes and references

1 G.-Q. Zhang, L.-J. Gao, H.-M. Chai and Y.-X. Ren, *ACS Omega*, 2021, **6**, 6810–6816.

2 Z. Sun, J. Sun, L. Xi, J. Xie, X. Wang, Y. Ma and L. Li, *Cryst. Growth Des.*, 2020, **20**, 5225–5234.

3 (*a*) L. Li, Q. Chen, Z. Niu, X. Zhou, T. Yang and W. Huang, *J. Mater. Chem. C*, 2016, **4**, 1900–1905; (*b*) Y. Shi, L. He, X. Wang, Z. Wu, N. Guo, H. Zhang, W. Wang and J. Cui, *J. Rare Earths*, 2020, **38**, 1231–1236; (*c*) M. Liu, H. Li, L. Bai, K. Zheng, Z. Zhao, Z. Chen, S. W. Ng, L. Ding and C. Zeng, *J. Hazard. Mater.*, 2021, **413**, 125291.

4 P. Jia, Z. Wang, Y. Zhang, D. Zhang, W. Gao, Y. Su, Y. Li and C. Yang, *Spectrochim. Acta, Part A*, 2020, **230**, 118084.

5 L. Liu, Y. Wang, R. Lin, Z. Yao, Q. Lin, L. Wang, Z. Zhang and S. Xiang, *Dalton Trans.*, 2018, **47**, 16190–16196.

6 Y. Sun, N. Zhang, Q. L. Guan, C. H. Liu, B. Li, K. Y. Zhang, G. H. Li, Y. H. Xing, F. Y. Bai and L. X. Sun, *Cryst. Growth Des.*, 2019, **19**, 7217–7229.

7 H. Yu, M. Fan, Q. Liu, Z. Su, X. Li, Q. Pan and X. Hu, *Inorg. Chem.*, 2020, **59**, 2005–2010.

8 P. Kumar, A. Deep and K.-H. Kim, *TrAC, Trends Anal. Chem.*, 2015, **73**, 39–53.

9 (*a*) S. Liu, M. Liu, M. Guo, Z. Wang, X. Wang, W. Cui and Z. Tian, *J. Lumin.*, 2021, **236**, 118102; (*b*) Y. Jiang, K. Zheng, Z. Liu, X. Yu, Q. Yang, T. Tang and C. Zeng, *Adv. Opt. Mater.*, 2022, **10**, 2102267.

10 B. Li, W. Wang, Z. Hong, E. S. M. El-Sayed and D. Yuan, *Chem. Commun.*, 2019, **55**, 6926–6929.

11 H. Wang, X. Wang, M. Liang, G. Chen, R.-M. Kong, L. Xia and F. Qu, *Anal. Chem.*, 2020, **92**, 3366–3372.

12 (*a*) R. Li, W. Wang, E. S. M. El-Sayed, K. Su, P. He and D. Yuan, *Sens. Actuators, B*, 2021, **330**, 129314; (*b*) J. Xue, Y. Wang, G. Yang and Y. Wang, *J. Rare Earths*, 2023, DOI: **10.1016/j.jre.2023.02.016**.

13 (*a*) X. Li, J. X. Tang, H. Liu, K. Gao, X. R. Meng, J. Wu and H. W. Hou, *Chem.–Asian J.*, 2019, **14**, 3721–3727; (*b*) M.-Q. Yang, C.-P. Zhou, Y. Chen, J.-J. Li, C.-H. Zeng and S. Zhong, *Sens. Actuators, B*, 2017, **248**, 589–596; (*c*) K. Zheng, Z.-Q. Liu, Y. Huang, F. Chen, C.-H. Zeng, S. Zhong and S. W. Ng, *Sens. Actuators, B*, 2018, **257**, 705–713.

14 C. C. Zhang, X. F. Ma, P. P. Cen, X. Y. Jin, J. H. Yang, Y.-Q. Zhang, J. Ferrando-Soria, E. Pardo and X. Y. Liu, *Dalton Trans.*, 2020, **49**, 14123–14132.

15 Y.-Q. Sun, Y. Cheng and X.-B. Yin, *Anal. Chem.*, 2021, **93**, 3559–3566.

16 X. Wang, Z. Jiang, C. Yang, S. Zhen, C. Huang and Y. Li, *J. Hazard. Mater.*, 2022, **423**, 126978.

17 F. Q. An, C. C. Zhang, L. J. Duan, X. Y. Liu, Z. Wang, X. Y. Jin and W. M. Song, *New J. Chem.*, 2019, **43**, 4800–4807.

18 H. H. Yu, M. Y. Fan, Q. Liu, Z. M. Su, X. Li, Q. Q. Pan and X. L. Hu, *Inorg. Chem.*, 2020, **59**, 2005–2010.

19 J. Zhang, Y. Huang, D. Yue, Y. Cui, Y. Yang and G. Qian, *J. Mater. Chem. B*, 2018, **6**, 5174–5180.

20 W.-M. Chen, X.-L. Meng, G.-L. Zhuang, Z. Wang, M. Kurmoo, Q.-Q. Zhao, X.-P. Wang, B. Shan, C.-H. Tung and D. Sun, *J. Mater. Chem. A*, 2017, **5**, 13079–13085.

21 C. Zhang, Y. Qin, L. Duan, L. Wang, Y. Wu, Y. Guo, W. Song and X. Liu, *Dalton Trans.*, 2022, **51**, 473–477.

22 L. Fan, W. Fan, B. Li, X. Liu, X. Zhao and X. Zhang, *Dalton Trans.*, 2015, **44**, 2380–2389.

23 J.-Z. Li, F. Bigdeli, X.-M. Gao, R. Wang, X.-W. Wei, X.-W. Yan, M.-L. Hu, K.-G. Liu and A. Morsali, *Inorg. Chem.*, 2019, **58**, 5397–5400.

24 W. Liu, D. Li, F. Wang, X. Chen, X. Wang and Y. Tian, *Opt. Mater.*, 2022, **123**, 111895.

25 X.-L. Lv, S. Yuan, L.-H. Xie, H. F. Darke, Y. Chen, T. He, C. Dong, B. Wang, Y.-Z. Zhang, J.-R. Li and H.-C. Zhou, *J. Am. Chem. Soc.*, 2019, **141**, 10283–10293.

26 (*a*) E. A. Dolgopolova, A. M. Rice, C. R. Martin and N. B. Shustova, *Chem. Soc. Rev.*, 2018, **47**, 4710–4728; (*b*) L.-L. Liu, C.-X. Yu, J. Sun, P.-P. Meng, F.-J. Ma, J.-M. Du and J.-F. Ma, *Dalton Trans.*, 2014, **43**, 2915–2924; (*c*) H. Li, Y. Han, X. Lv, S. Du, H. Hou and Y. Fan, *CrystEngComm*, 2013, **15**, 3672–3677; (*d*) J. Huang, H. Li, J. Zhang, L. Jiang and C. Y. Su, *Inorg. Chim. Acta*, 2012, **388**, 16–21; (*e*) S.-J. Liu, L. Xue, T.-L. Hu and X.-H. Bu, *Dalton Trans.*, 2012, **41**, 6813–6819; (*f*) J. Y. Lu, *Coord. Chem. Rev.*, 2003, **246**, 327–347.

27 J. R. Lakowicz, *Principles of Fluorescence Spectroscopy*, Kluwer Academic/Plenum Publishers, New York, 2nd edn, 1999.

28 W. Yan, C. L. Zhang, S. G. Chen, L. J. Han and H. G. Zheng, *ACS Appl. Mater. Interfaces*, 2019, **9**, 1629–1634.